Simultaneous Bayesian inversion for effective anisotropic parameters and microseismic event locations: a physical modelling study

Hongliang Zhang, Jan Dettmer, Joe Wong, and Kristopher A. Innanen

ABSTRACT

To account for anisotropy caused by the presence of a set of aligned vertical fractures in a finely horizontally layered background medium, we present an inversion procedure to simultaneously estimate microseismic event locations and the parameters of an orthorhombic (ORT) anisotropic medium property model. The procedure employs Bayesian inference via Markov-chain Monte Carlo (McMC) sampling with parallel tempering, and principal component diminishing adaptation, to ensure efficient sampling of the parameter space. This approach provides a nonlinear uncertainty quantification, by approximating the posterior probability density with an ensemble of model-parameter sets for effective anisotropic parameters, microseismic event locations and horizontal locations of perforation shots. The noise standard deviation is also treated as an extra unknown in the inversion. To investigate the effects of model simplification, e.g., neglect of horizontal-layering induced vertical transverse isotropy (VTI), we also consider a simpler, horizontal transverse isotropic (HTI), parametrization. The inversion is carried out for simulated data and data from a seismic physical laboratory model. Results suggest that, for field microseismic data processing, neglect of VTI signal caused by horizontal layering in fractured reservoirs may lead to systematic errors in microseismic event locations. Synthetic experiments further demonstrate that the acquisition geometry significantly impacts the resolution of event origin times, event depths, and effective velocity parameters. In addition, resolving these parameters requires an aperture size which may not be practical for field monitoring. Finally, we demonstrate that precise perforation-shot timing information and the incorporation of a vertical downhole array into the small-aperture surface array both reduce the requirement for large array apertures.

INTRODUCTION

As a well-stimulation technique, hydraulic fracturing has been widely applied in unconventional reservoirs to enhance reservoir permeability and production. The induced seismic response to fluid injection in hydrocarbon and geothermal reservoirs can be recorded by microseismic monitoring arrays, and the located microseismic events aid in mapping hydraulic fractures, characterizing fracture-rupture processes and providing insights into geomechanical processes (Shapiro et al., 2006; Baig and Urbancic, 2010; Eyre and van der Baan, 2017; Zhang et al., 2019).

The accuracy of estimated microseismic event locations relies on the state of knowledge about the surrounding velocity structure. A 3D velocity model can account for detailed spatial variations of velocity, but building such model often requires 3D seismic data and/or tomography techniques (Kissling, 1988; Cameron et al., 2007). In many cases, in the absence of sufficient 3D data, layered velocity models are assumed when locating microseismic events (e.g., Warpinski et al., 2005; Akram and Eaton, 2017). Perforation or string

shots are often used to calibrate the initial velocity model obtained from smoothed well-log measurements by either perturbing the velocity values in specific layers or introducing anisotropic parameters (Maxwell et al., 2010). Many approaches to optimize the 1D velocity model have been suggested in previous studies. For example, Occam's inversion (Pei et al., 2008) and fast simulated annealing inversion (Pei et al., 2009) have been adopted to optimize flat-layered velocity models by minimizing arrival-time misfit. Zhang et al. (2016) applied differential evolution to calibrate 1D velocity models using station-pair differential arrival times. The neighborhood algorithm (Sambridge, 1999a,b) was applied to calibrate the velocity model before microseismic events were located with a master-station method (Tan et al., 2018), in which a hybrid objective function that combines misfits for both arrival times and arrival-time difference between P- and S-waves was used. A number of studies have also documented simultaneous inversions for velocity structures and hypocentre locations (e.g., Pavlis and Booker, 1980; Thurber, 1992; Block et al., 1994; Jansky et al., 2010; Blias and Grechka, 2013. However, the practicality of such approaches may be limited because of insufficient constraints on the velocity model, poor aperture coverage of networks, and low signal-to-noise ratios (Eaton and Forouhideh, 2011; Tan et al., 2018).

The actual earth is complex, and a significant degree of transverse velocity anisotropy is common in most sedimentary formations due to layering, mineralogy and natural fracturing (Warpinski et al., 2009). Failure to account for such anisotropy may lead to significant event-location errors (Erwemi et al., 2010; Maxwell et al., 2010; Woerpel, 2010). In some shale reservoirs, strong VTI is common, and Thomsen anisotropic parameters for these media can be estimated through inversion (e.g., King and Talebi, 2007; Li et al., 2013; Zhang and Li, 2013; Jarillo Michel and Tsvankin, 2017). For example, Zhang and Li (2013) developed a linearized iterative approach to estimate Thomsen parameters based on P-wave arrival times of microseismic data recorded on a buried array. However, the inverted anisotropic parameters were found to be sensitive to initial event-depth estimates, an issue a fully nonlinear approach can address. A simultaneous inversion of event location and anisotropic tomography was developed using differential arrival times and differential backazimuths for 1D layered VTI media (Li et al., 2013). The accuracy of this method depends strongly on the ray-angle coverage. Jarillo Michel and Tsvankin (2017) extended an elastic waveform-inversion algorithm to velocity-model building from microseismic data for 2D gridded VTI media, but this algorithm has relatively small error tolerance (on the order of 5%) in the initial values of some model parameters (P-wave horizontal velocity V_{hor}, S-wave vertical velocity V_{S0}, and anisotropy coefficient η). Horizontal transverse isotropy is typically caused by aligned vertical fractures. It is common in Earth's crust due to tectonic stress and/or hydraulic fracturing (Grechka, 2005; Chichinina et al., 2013). The presence of HTI can have a considerable influence on microseismic event location (Van Dok et al., 2011; Chen et al., 2013). Nevertheless, only few studies have conducted inversion for anisotropic parameters and microseismic event locations in HTI media. For example, Yaskevich and Duchkov (2012, 2013) showed that HTI parameters can be constrained in the simultaneous inversion of event location and anisotropic velocity model with downhole microseismic data. Since the geometry of perforation shots influences the accuracy of anisotropic parameter estimation, the inclusion of wide-angle perforation shots can improve the robustness of the inversion.

Fractured reservoirs typically present a combination of layering-caused VTI and fracture-

caused HTI. This combination of effects can be characterized by ORT anisotropy (Zhang and Li, 2013; Chen et al., 2019). For ORT media, Yuan and Li (2017) estimated anisotropic parameters simultaneously with microseismic event locations using S-wave splitting measurements from downhole microseismic data. With a synthetic downhole microseismic dataset, Shimoda et al. (2016) tested the effectiveness of the iterative gradient-based Levenberg-Marquardt algorithm to calculate anisotropic parameters for the tilted ORT model.

Most inversion algorithms mentioned thus far employ various deterministic linear or linearized inversion approaches (Husen and Hardebeck, 2010). To rigorously quantify the uncertainties of model parameters requires careful treatment of data errors and a variety of Bayesian approaches have been proposed for velocity calibration and/or hypocentre estimation. Most of these approaches involve simple velocity models: constant velocity (e.g., Purba et al., 2020), 1D layered isotropic velocity (e.g., Hirata and Matsu'ura, 1987; Poliannikov et al., 2013, 2014; Gesret et al., 2015; Zhang et al., 2018; Ryberg and Haberland, 2019), and 1D layered models with linear velocity gradients in each layer (e.g., Zhang et al., 2017). However, Bayesian inversion can also be applied in 3D local earthquake tomography (velocity structure and hypocentre locations are unknowns) at considerable computational cost (Piana Agostinetti et al., 2015).

In this study, we account for ORT anisotropy caused by the presence of aligned vertical fractures in finely horizontally layered background media in a nonlinear Bayesian inversion for simultaneous source-location determination and velocity estimation. We examine the effects of model choice by considering both ORT and HTI velocity models. The HTI model ignores the anisotropic effects of horizontal-layering induced VTI but also requires fewer model parameters. The inversion employs McMC sampling with parallel tempering and diminishing adaption of a principal axes proposal density (Dosso et al., 2014) to ensure efficient sampling. In particular, the adaptation is specific to the temperature of the chain. We apply our approach to both computer simulated data and laboratory observations. The computer simulations are carried out to examine the effects of model choice and acquisition geometries on parameter estimation and uncertainties. The laboratory observations are acquired with a physical modelling experiment which includes an analog anisotropic layer built by a phenolic CE material. The laboratory experiment also includes analogs for perforation shots and microseismic events. Comparisons are made between the results obtained with the two anisotropic-medium approximations (i.e., HTI and ORT) for the phenolic layer.

THEORY AND ALGORITHM

Quasi-P-wave (qP-wave) group velocity in HTI and ORT media

The simplest effective wave-propagation model of a formation with a set of aligned vertical fractures is HTI, in which the symmetry axis is perpendicular to the fracture orientation (Bakulin et al., 2000). For HTI media, Byun et al. (1989) approximated the qP-wave group velocity as a function of ray angle with a truncated Fourier cosine transform, which is given by

$$V_P^{-2}(\phi) = a_0 + a_1 cos^2\phi - a_2 cos^4\phi, \tag{1}$$

where ϕ is the ray angle with respect to the symmetry axis. The Fourier coefficients a_0, a_1 and a_2 can be represented by three observable parameters

$$a_0 = V_{90}^{-2}, \tag{2}$$

$$a_1 = 4V_{45}^{-2} - 3V_{90}^{-2} - V_0^{-2}, \tag{3}$$

and

$$a_2 = 4V_{45}^{-2} - 2V_{90}^{-2} - 2V_0^{-2}, \tag{4}$$

where V_0, V_{45} and V_{90} are qP-wave group velocities at group angles of 0° 45° and 90°, respectively. Once the three Fourier coefficients are calculated (equations (2–4)), evaluating group velocity is straightforward for any ray path within the HTI medium (Kumar et al., 2004).

Stress-induced, vertically aligned fractures often exist within horizontally layered sedimentary formations, where the horizontal layering may lead to layering-caused anisotropy known as VTI (Hornby et al., 1994; Chen et al., 2019). However, vertically aligned fractures also cause HTI effects. The combination of these types of anisotropy in the background medium can be modelled by ORT anisotropy (Zhang and Li, 2013; Chen et al., 2019). In ORT media, the density-normalized stiffness matrix **A** has nine independent stiffness coefficients

$$A = \begin{bmatrix} A_{11} & A_{12} & A_{13} & & & \\ A_{21} & A_{22} & A_{23} & & & \\ A_{31} & A_{32} & A_{33} & & & \\ & & & A_{44} & & \\ & & & & A_{55} & \\ & & & & & A_{66} \end{bmatrix}, \tag{5}$$

where the main-diagonal stiffness coefficients are related to the quasi-body wave velocities along three axes in cartesian coordinates. For i = 1, 2, 3, the A_{ii} are related to the qP-wave velocities V_{11}, V_{22}, and V_{33} along the x_1, x_2, and x_3 axes, respectively. These velocities are given by $A_{ii} = V_{ii}^2$. For i = 4, 5, 6, the A_{ii} are related to qS-wave velocities, given by $A_{44} = V_{23}^2 = V_{32}^2$, $A_{55} = V_{13}^2 = V_{31}^2$ and $A_{66} = V_{12}^2 = V_{21}^2$, where V_{ij} ($i \neq j$) denotes a qS-wave propagating along x_j axis and polarized along the x_i axis. The off-diagonal elements are not directly related to the phase or group velocities of quasi-body waves.

Using the density-normalized stiffness coefficients for ORT media, the qP-wave group velocity can be approximated by linearization (Song and Every, 2000; Daley and Krebes, 2016) as

$$\frac{1}{V_P^2(\mathbf{N})} = \frac{N_1^2}{A_{11}} + \frac{N_2^2}{A_{22}} + \frac{N_3^2}{A_{33}} - \frac{E_{12}N_1^2N_2^2}{A_{11}A_{22}} - \frac{E_{13}N_1^2N_3^2}{A_{11}A_{33}} - \frac{E_{23}N_2^2N_3^2}{A_{22}A_{33}}, \tag{6}$$

where $\mathbf{N} = (N_1, N_2, N_3)$ is the unit vector in the ray direction that can be represented in polar coordinates as $\mathbf{N} = (sin\Theta cos\Phi, sin\Theta sin\Phi, cos\Phi)$. Here, Θ and Φ are the polar and azimuthal angles measured from positive x_3 and x_1 axes, respectively. The $E_{ij}(ij = 12, 13, 23)$ are anellipsoidal terms specifying deviations of the slowness or ray surface from the ellipsoidal in the ij symmetry plane (Daley and Krebes, 2016). The three anellipsoidal terms are defined as

$$E_{12} = 2(A_{12} + 2A_{66}) - (A_{11} + A_{22}), \tag{7}$$

$$E_{13} = 2(A_{13} + 2A_{55}) - (A_{11} + A_{33}), \tag{8}$$

and

$$E_{23} = 2(A_{23} + 2A_{44}) - (A_{22} + A_{33}). \tag{9}$$

The inversion algorithm used in this study is based on P-wave first arrivals only. Therefore, it is not possible to resolve all nine stiffness coefficients, in particular those related to qS-wave velocities (A_{44}, A_{55}, A_{66}). Therefore, we define three parameters $B_1 = 2(A_{12} + 2A_{66})$, $B_2 = 2(A_{13} + 2A_{55})$, and $B_3 = 2(A_{23} + 2A_{44})$ to reduce parametrization complexity. Despite the fact that the stiffness matrix cannot be fully resolved by P-wave data, the qP-wave group velocity along any ray direction can be obtained from equation (6) by employing our modified model with six independent parameters (V_{11}, V_{22}, V_{33}, B_1, B_2, B_3), which is sufficient for this study.

Simultaneous Bayesian inversion for effective velocity parameters and microseismic event locations in anisotropic media

In conventional microseismic data processing, an initial velocity model is typically obtained from nearby well-log data. In addition, perforation shots are often available and assumed to have known locations. The perforation shots are then used to calibrate the velocity model. With the calibrated velocity model, microseismic events are located based on either arrival-time or waveform data. In this work, we apply probabilistic nonlinear inversion for concurrent estimation of anisotropic properties and microseismic event locations in HTI and ORT media. The Bayesian inference is carried out by McMC sampling

with parallel tempering (Geyer, 1991; Dettmer and Dosso, 2012; Sambridge, 2014) and diminishing adaption of a principal axes proposal density (Dosso et al., 2014).

According to Bayes' theorem, the posterior probability density (PPD) $P(\mathbf{m}|\mathbf{d})$ is expressed as

$$P(\mathbf{m}|\mathbf{d}) \propto P(\mathbf{d}|\mathbf{m})P(\mathbf{m}), \tag{10}$$

where $\mathbf{m}$ and $\mathbf{d}$ are model and data vectors, respectively. For measured data $\mathbf{d}^{obs}$, $P(\mathbf{d}^{obs}|\mathbf{m})$ is interpreted as the likelihood function $L(\mathbf{m})$. The prior probability is given by $P(\mathbf{m})$. Under the assumption of Gaussian-distributed errors, the likelihood function is

$$L(\mathbf{m}, \mathbf{C}_d) = \frac{1}{(2\pi)^{N/2}|\mathbf{C}_d|^{1/2}} \exp[-\frac{1}{2}(\mathbf{d} - g(\mathbf{m}))^T \mathbf{C}_d^{1/2}(\mathbf{d} - g(\mathbf{m}))], \tag{11}$$

where N is the number of observed data, g is the forward model in either HTI or ORT media, and $\mathbf{C}_d$ represents the data covariance matrix which is often unknown. If noise is assumed stationary and the off-diagonal terms of the covariance matrix are assumed negligible, equation (11) becomes

$$L(\mathbf{x}) = \frac{1}{(2\pi)^{N/2}|\sigma_d^N} \exp[-(\mathbf{d} - g(\mathbf{m}))^T(\mathbf{d} - g(\mathbf{m}))/(2\sigma_d^2)], \tag{12}$$

where the unknown standard deviation σ_d can be estimated by McMC sampling and is here included in the new model vector $\mathbf{x} = [\mathbf{m}, \sigma_d]$ in the inversion.

Parallel tempering (Earl and Deem, 2005; Dettmer and Dosso, 2012) employs a series of parallel and interacting Markov-chains with likelihood functions tempered by a parameter $0 < \beta \leq 1$. According to the Metropolis-Hastings criterion, the acceptance probability for the perturbed model $\mathbf{x}'$ is

$$\alpha(\mathbf{x}'|\mathbf{x}) = \min\{1, \frac{Q(\mathbf{x}|\mathbf{x}')}{Q(\mathbf{x}'|\mathbf{x})} \frac{P(\mathbf{x}')}{P(\mathbf{x})} [\frac{L(\mathbf{x}')}{L(\mathbf{x})}]^\beta\}\}, \tag{13}$$

where Q is the proposal density. We assume a symmetric Q ($Q(\mathbf{x}'|\mathbf{x}) = Q(\mathbf{x}|\mathbf{x}')$) and uniform bounded priors. Therefore, equation (13) simplifies as

$$\alpha(\mathbf{x}'|\mathbf{x}) = \min\{1, [\frac{L(\mathbf{x}')}{L(\mathbf{x})}]^\beta\}, \tag{14}$$

where the tempering parameter β in equation (14) denotes the inverse temperature of this chain. Chains with small β values have increased probability to accept models with

low likelihood, thus can sample over broad regions in the parameter space. On the contrary, the sampling at a high β value is prone to be trapped in local modes (Dosso et al., 2014). The acceptance for chain swaps is based on the Metropolis-Hastings criterion, where the acceptance probability for the exchange of model vector $\mathbf{x}_i$ with tempering parameter β_i and model vector $\mathbf{x}_j$ with β_j is

$$\begin{aligned}\alpha[(\mathbf{x}_j,\beta_i),(\mathbf{x}_i,\beta_j)|(\mathbf{x}_i,\beta_i),(\mathbf{x}_j,\beta_j)] &= \min\{1,\frac{P(\mathbf{x}_j)[L(\mathbf{x}_j)]^{\beta_i}}{P(\mathbf{x}_i)[L(\mathbf{x}_i)]^{\beta_i}}\frac{P(\mathbf{x}_i)[L(\mathbf{x}_i)]^{\beta_j}}{P(\mathbf{x}_j)[L(\mathbf{x}_j)]^{\beta_j}}\} \\ &= \min\{1,[\frac{L(\mathbf{x}_i)}{L(\mathbf{x}_j)}]^{(\beta_j-\beta_i)}\}.\end{aligned} \tag{15}$$

To overcome the inefficiency due to correlated parameters, we follow Dosso et al. (2014) to adapt the proposal distribution during sampling. The proposal distribution is considered as a univariate Gaussian distribution along principal axes (PAs) of the parameter space. The direction and effective perturbation length scale are obtained through a singular-value decomposition of the model covariance matrix which is initialized with a linearized estimate based on a Laplace approximation around a starting model. This estimate is subsequently updated by the McMC samples and the adaptation is diminished over time. By rotating parameter vectors into PA space, correlated parameters are efficiently sampled in terms of step direction and step sizes are given by the singular values. Importantly, the proposal for each Markov chain is adapted individually. Therefore, proposals for small β values generally adapt to larger step sizes resulting in appropriate scaling for all chains.

As described previously, three velocity parameters (V_0, V_{45}, V_{90}) describe HTI media based on the approximation by Byun et al. (1989), and six independent parameters (V_{11}, V_{22}, V_{33}, B_1, B_2, B_3) constrain ORT media. However, the orientations of symmetry axes and principal axes are also unknown. Therefore, we include an additional unknown in the inversion. For HTI media, this unknown is the deviation angle (θ) of the symmetry axis. For ORT media, this unknown is the angle between the x_1 axis and the x axis in the coordinate system used for data acquisition.

In field data, locations of perforation shots are generally not known accurately due to measurement errors and engineering challenges. Therefore, we treat these locations as unknown but apply prior distributions that reflect reasonable location uncertainty. Instead of assigning broad uniform priors such as those for microseismic events, we assign narrow distributions around the recorded perforation-shot locations as priors. Furthermore, the inversion also considers the standard deviation (σ_d) of the noise as unknown. Origin times (t_0) for perforation shots and microseismic events are generally poorly known or unknown and are included as unknown model parameters in the inversion. Based on these considerations, the model vector for HTI media is **x** = [θ, V_0, V_{45}, V_{90}, $t_0^{(1)}$, $x^{(1)}$, $y^{(1)}$, $z^{(1)}$, $\dots$, $t_0^{(K)}$, $x^{(K)}$, $y^{(K)}$, $z^{(K)}$, σ_d], where K is the total number of events including perforation shots and microseismic events. For the ORT model, **x** is [θ, V_{11}, V_{22}, V_{33}, B_1, B_2, B_3, $t_0^{(1)}$, $x^{(1)}$, $y^{(1)}$, $z^{(1)}$, $\dots$, $t_0^{(K)}$, $x^{(K)}$, $y^{(K)}$, $z^{(K)}$, σ_d].

PHYSICAL MODELLING SETUP

To examine the response and effectiveness of the proposed simultaneous inversion algorithm, an experiment is designed to generate simulated microseismic data based on a physical model. This experiment is a miniaturized version with 1:10,000 spatial and temporal scaling of microseismic field monitoring. In the following, we refer to scaled quantities by applying the scaling factor to the actual experiment quantities. The acquisition geometry is an analog of star-shaped surface-receiver array. In the physical model, we use a phenolic CE laminate material as an analog of the anisotropic medium. The anisotropy is addressed by HTI and ORT models for data predictions in the inversion. Due to practical constraints for the placement of transducers near and within solid targets, the phenolic slab is immersed in a water tank, and sources and receivers are placed in water (Figure 1). Specifically, receivers are placed $\sim$233 m above the top of the phenolic layer, and sources are placed 110 to 145 m below the bottom of the slab. Figure 1 shows the acquisition geometry, in which eight simulated perforation shots (assumed to be within two horizontal wells) are available, and 11 simulated microseismic events have unknown locations to be estimated by the inversion. The surface-receiver array consists of five receiver lines, each line with 20 evenly spaced receivers. The horizontal receiver distance from the well head (assumed to be located at the coordinate origin) ranges from 40 to 760 m. Depths of perforation shots and microseismic events range between 810 and 845 m. The Bayesian inversion is based on P-wave first arrivals, and cross-correlation is used for P-wave arrival-time picking. In Figure 2, waveforms for a typical perforation shot recorded by the star-like array are plotted. In the forward modelling, P-wave travel times are calculated based on a ray-shooting algorithm for the three-layer model shown in Figure 1.

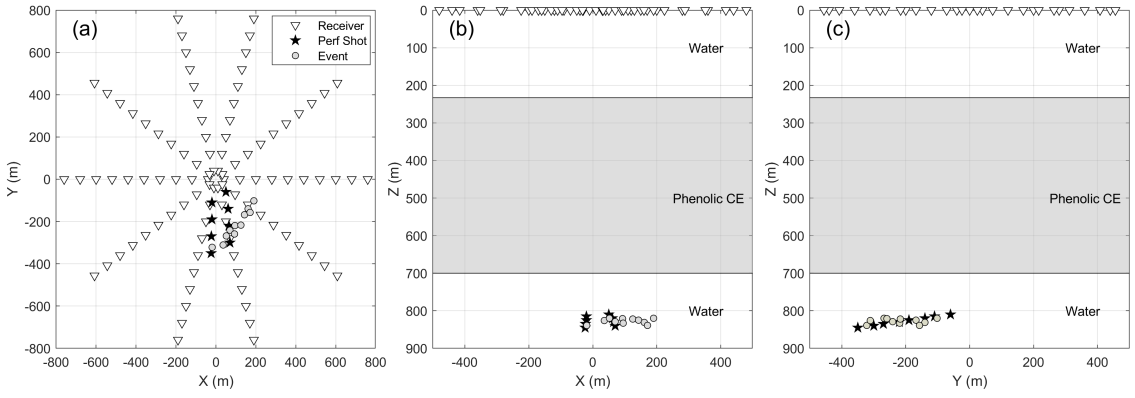

FIG. 1. Map view (a) and side views (b), (c) of the acquisition geometry for the physical modelling experiment. Stars, circles and triangles denote the simulated perforation shots, microseismic events and receivers, respectively.

In the physical model, we use piezoelectric pins with diameters of $\sim$2.36 mm to act as both sources and receivers. This scales to a size of $\sim$23.6 m, which causes a measurement error for the perforation-shot locations of comparable magnitude. Therefore, even with known perforation-shot locations, we assign narrow uniform priors to reflect uncertainty (horizontally $\pm$ 50 m around the recorded acquisition-system location). Previous studies have shown that the inverted vertical locations under a surface array have relatively large

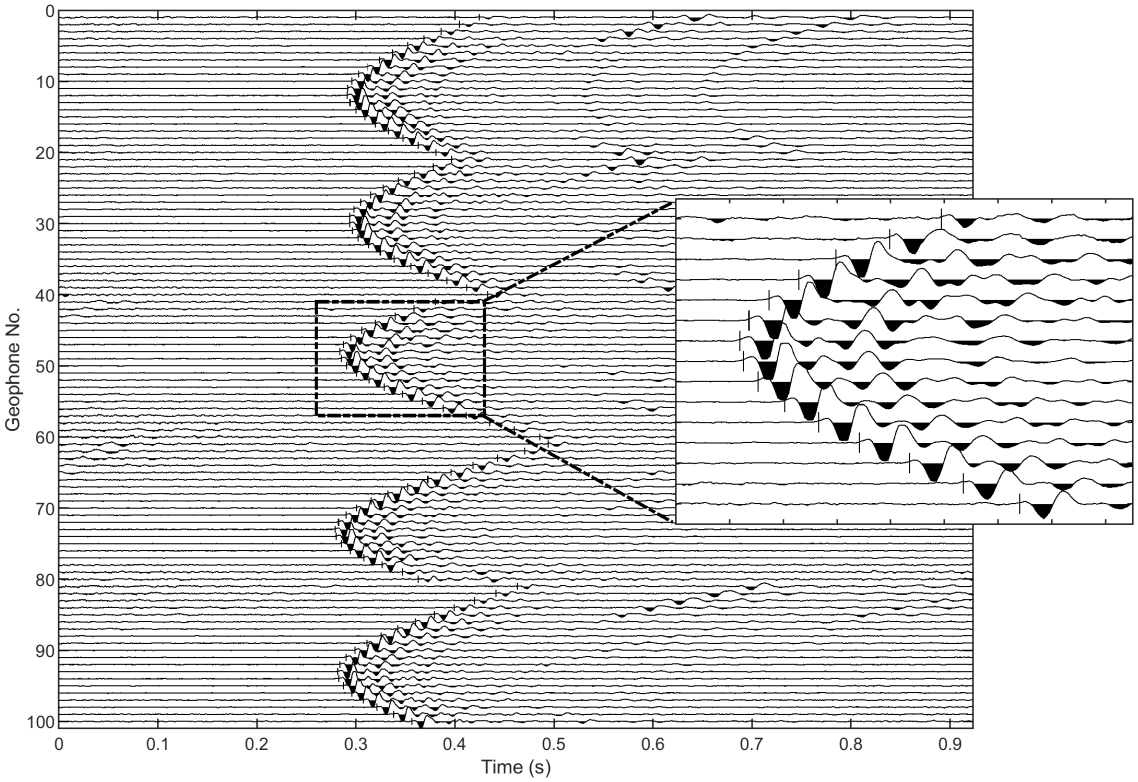

FIG. 2. Waveform recordings (AGC applied) for a typical event. The picked P-wave first-arrival times are marked by vertical lines. The inset shows waveforms and picked P-wave arrival times at one receiver line.

uncertainty especially when only one phase (P-wave) is used in the inversion (Eisner et al., 2009, 2010). Therefore, we treat perforation-shot depths as known in the simultaneous inversion. The depths to the top and bottom of the phenolic layer are assumed to be known, and the velocity of water is also assumed to be known. For anisotropic parameters and microseismic event locations, we assign broad uniform priors: microseismic-event locations are assigned priors from -800 to 800 *m* in the horizontal, and between 700- and 900-*m* depth. The HTI parameters have prior bounds of [0°,180°]for θ, [2500 *m/s*, 3500 *m/s*] for V_0, [2800 *m/s*, 4200 *m/s*] for V_{45} and [2800 *m/s*, 4200 *m/s*] for V_{90}. For the ORT medium, the priors are [0°, 180°] for θ, [2500 *m/s*, 3500 *m/s*] for V_{11}, [3000 *m/s*, 4000 *m/s*] for V_{22}, V_{33}, and [5×10^6 m^2/s^2, 5×10^7 m^2/s^2] for B_1, B_2, B_3. These priors for V_{11}, V_{22}, V_{33}, B_1, B_2 and B_3 are chosen based on the density-normalized stiffness matrix for the similar phenolic slab estimated by Mahmoudian (2013). In the physical modelling process, since origin times (or times) of both perforation shots and microseismic events are known, we first consider them as known parameters in the inversion then compare the results obtained by treating them as extra model parameters.

COMPUTER SIMULATION RESULTS

To investigate the performance of the algorithm, especially the robustness to different noise levels and the effects of array aperture on the inversion results, we apply the algorithm to simulated data with known true models. We use the same acquisition geometry

and same locations of simulated perforation shots and microseismic events as in Figure 1. In the simulation study presented here, we first consider the case with known origin times to examine the effects of noise on two sets of inversion results with HTI- and ORT-model approximations for the anisotropic medium. Whereas, for the case with unknown origin times, the inversion may yield unstable results for some model parameters due to insufficient array apertures. The effects from array aperture will be further illustrated in the simulation study. In addition, we also present two simulations to help better constrain model parameters, especially event origin times and depths. These two simulations are carried out with triggered (i.e., with known origin times) perforation shots and with a hybrid monitoring array, respectively.

We assume velocity structure as shown in Figure 1 with an anisotropic material in the middle of two water layers. To mimic the physical modelling case, we assign values of 2925 *m/s*, 3365 *m/s* and 3576 *m/s* for V_{11}, V_{22} and V_{33}, respectively. These values are selected based on Cheadle et al. (1991), in which a similar phenolic CE material that exhibits orthorhombic anisotropy was used. True values of B_1, B_2 and B_3 are set to be 1.95×10^7 m^2/s^2, 2.05×10^7 m^2/s^2 and 2.2×10^7 m^2/s^2, respectively. We assume the x_1 axis (horizontal slow P-wave direction, i.e., direction for V_{11}) of the anisotropic block to be parallel to the y axis of the acquisition coordinates, i.e., θ is 90°.

HTI model versus ORT model

The P-wave arrival times are modelled assuming the ORT medium and are contaminated by zero-mean, Gaussian-distributed noise. For microseismic data, picking errors are typically a few milliseconds (Eisner et al., 2009; Akram and Eaton, 2016). Nevertheless, we examine a large range of standard deviations to test the robustness of the proposed algorithm. Five sets of noise with standard deviations of 2 *ms*, 5 *ms*, 10 *ms*, 15 *ms* and 20 *ms* are added to the modelled arrival times to generate five simulated data sets. We carry out the inversion with both the ORT and HTI forward models. Therefore, this simulation study can also be used to investigate the effects caused by model simplification, i.e., the ignoring VTI effects caused by horizontal layering in a reservoir with a set of vertically aligned fractures. For the case where the HTI forward model is employed, theory errors also exist due to HTI forward model being inconsistent with the ORT assumption used to generate data.

The marginal distributions of model parameters are found to be Gaussian-like. Figures 3 shows the 95% credibility intervals (CIs) for errors in inverted horizonal and vertical event locations of two typical microseismic events (the first two rows) and two typical perforation shots (the last two rows) at the various noise levels. In general, the uncertainty becomes large with increasing noise for both forward models, and the widths of CIs at the same noise level are similar. Despite the increasing uncertainty, robust results are retrieved even for the case with a noise standard deviation of 20 *ms*. The x locations and depths obtained with the HTI forward model exhibit systematic shifts from the true values, especially for the microseismic events. The use of an HTI model tends to yield biased results with larger x locations and smaller depths than true values. For example, at noise level of 2 *ms*, mean absolute errors between values at modes of posterior marginals and true values are 6.3 *m* and -2.1 *m* for x location and depth with the HTI-model approximation, respectively. As

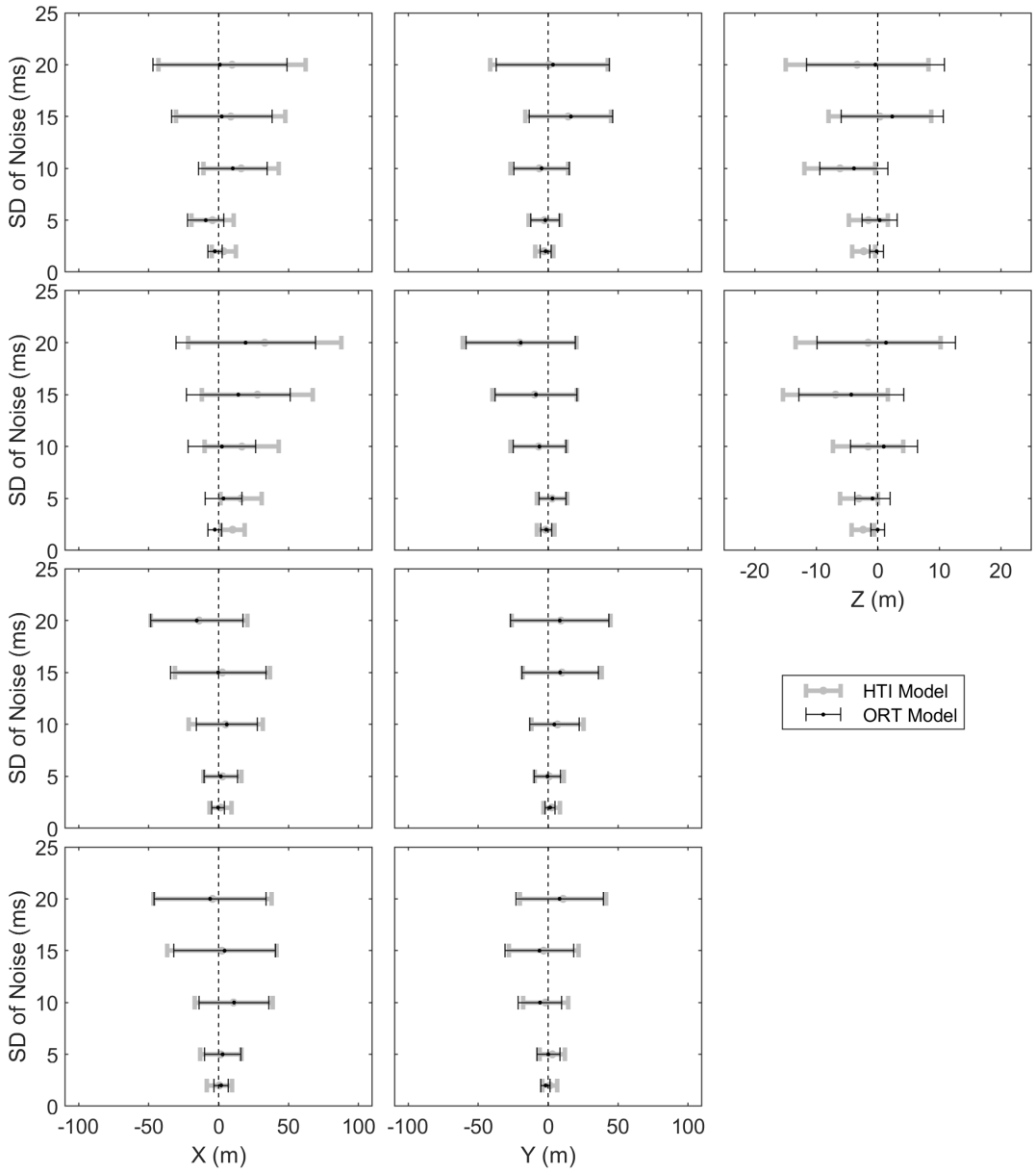

FIG. 3. 95% CIs for errors in estimated x, y and z locations for two typical microseismic events (the first two rows) and two typical perforation shots (the last two rows) using HTI-model and ORT-model approximations.

a comparison, mean absolute errors are -0.3 m and 0.1 m for the case with ORT-model approximation. In the simulation, the P-wave velocities along x, y and z directions are set to be 3365 *m/s*, 2925 *m/s* and 3576 *m/s* (i.e., V_{22}, V_{11} and V_{33}), respectively. In the HTI-medium assumption, the symmetry axis is along y axis, i.e., the horizontal slow P-wave direction. While velocities along x and z directions are the same under this approximation because both of them are perpendicular to the symmetry axis. As a result, the inversion yields a value of V_{90} (i.e., velocities along x and z directions) between V_{11} and V_{33} (shown in Figure 4 (a)), that is, the resulting velocity along the x axis is larger than the true velocity

(V_{22}), while the inferred velocity along the z axis is smaller than the true value (V_{33}). Therefore, the systematic shifts observed in Figures 3 can be explained by the model error due to the HTI approximation, and these shifts are proportional to the velocity difference along x and z directions. Therefore, the magnitude of errors will depend on the strength of anisotropy. In the simulation, the case with a standard deviation of 2 *ms* is closet to typical field data. For this case, comparing results for HTI and ORT forward models show that the ORT model generates solutions at the modes of posterior marginals closer to true values than solutions with the HTI model (shown in Figure 3).

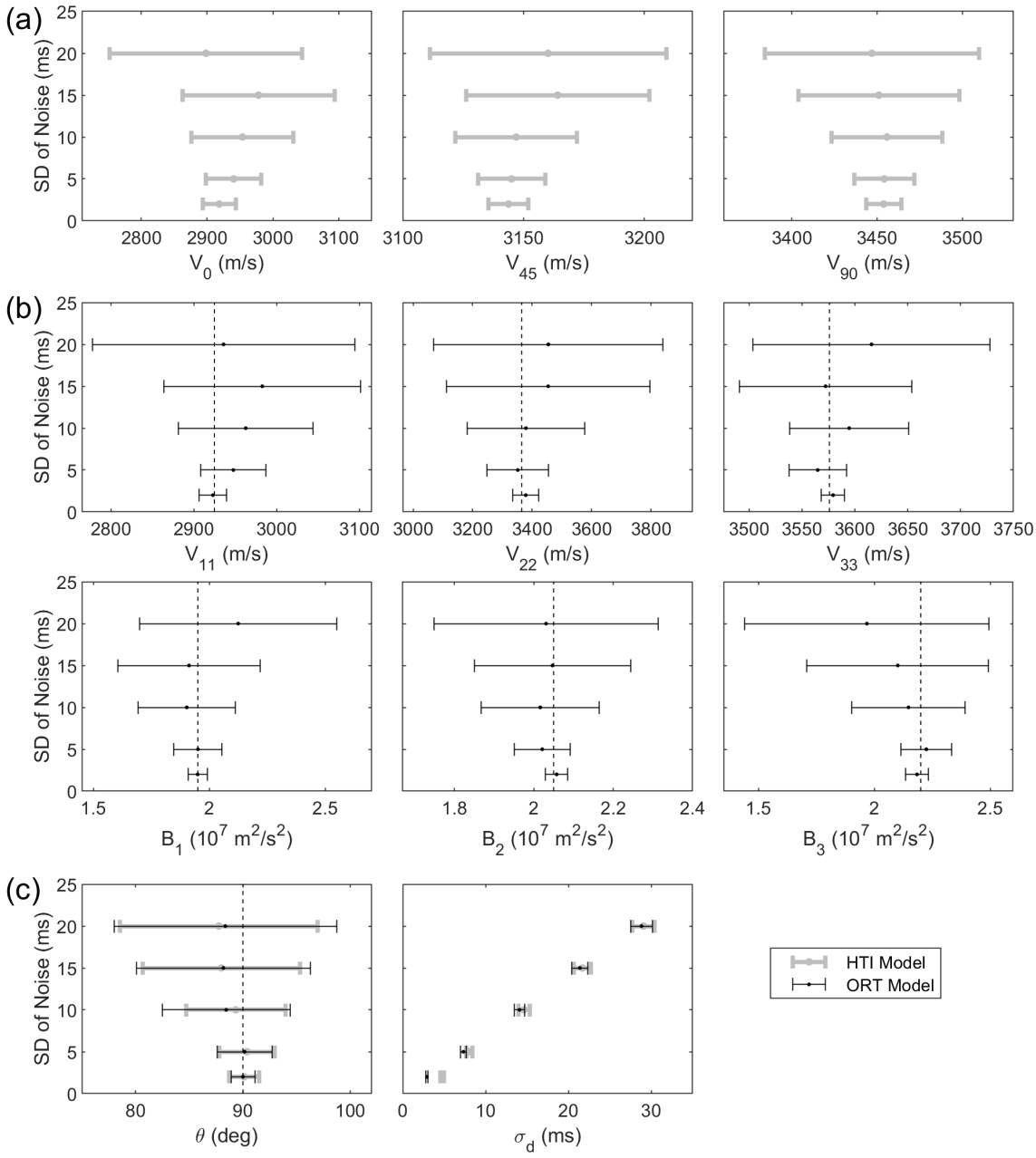

FIG. 4. 95% CIs of estimated anisotropic parameters (except θ) of (a) HTI model and (b) ORT model, (c) deviation angles (θ) of symmetry axis and x_1 axis from the x axis in the coordinate system as well as the noise standard deviation (σ_d).

Figure 4 shows 95% CIs for the estimated anisotropic parameters of HTI and ORT models, and noise standard deviations. Similar to the inversion results for event locations, the uncertainty regions for both cases are found to be proportional to noise levels. In addition, both cases yield robust and similar results for θ (shown in Figure 4 (c)). We also notice that the posterior marginals for V_0 in Figure 4 (a) are also highly similar to those for V_{11} in Figure 4 (b), that is because both of them represent the velocity along the y axis. In general, at all levels of noise considered in the simulation, both inversions yield robust results for anisotropic parameters. In comparison, the uncertainty regions for V_{22} are larger than those of other velocities (i.e., V_0, V_{45}, V_{90}, V_{11}, V_{33}). Therefore, uncertainty quantification is important for quantitative interpretation of results. In addition, for each noise level, the HTI-model approximation yields larger mode of posterior marginal for noise standard deviation than ORT model, which is mainly caused by the model error. To examine residual errors further, we estimate P-wave first arrival times for all perforation shots and microseismic events using the maximum a posteriori (MAP) model parameters and compute residuals for the simulation with noise level of 2 *ms*. Figure 5 presents residual histograms for both inversions with HTI and ORT models. The ORT model produces significantly smaller residuals with 95% CIs of [-4.0, 4.1] *ms*. In addition, the ORT residuals appear unbiased and the distribution is of Gaussian shape. In contrast, the 95% CIs for the HTI model are wider with values of [-6.3, 6.2] *ms*. Importantly, the HTI model produces a residual distribution that is not zero mean and asymmetric, indicating that the model cannot produce fits that are consistent with the assumption of Gaussian-distributed noise.

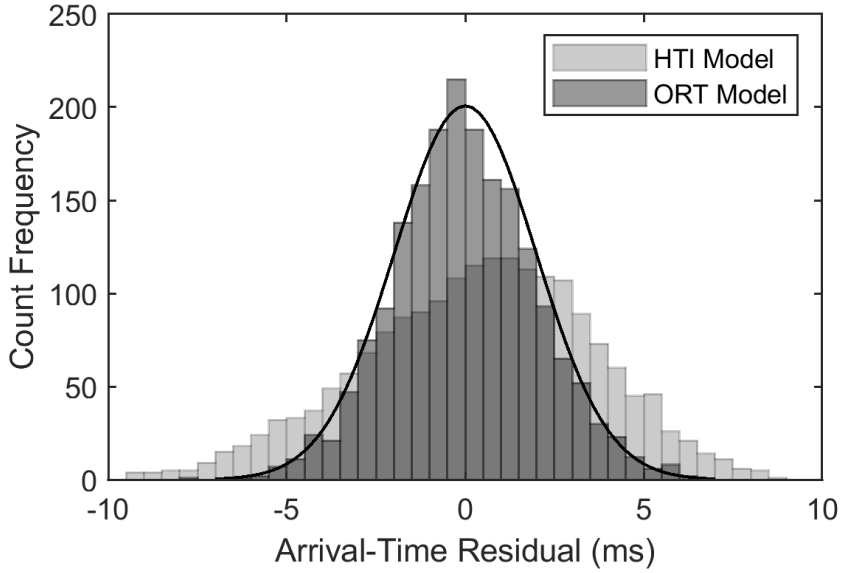

FIG. 5. Histograms of arrival-time residuals using HTI and ORT models for the simulation with noise level of 2 *ms*. The best-fitting Gaussian distribution for the result with ORT model is represented by the black line.

We also carry out a simulation by taking the depths of perforation shots as unknown parameters with uniform priors of $\pm$ 25 *m* around the true values. Due to the similarity between the two sets of results using HTI and ORT models, we only present the results with ORT model here. Posterior marginals of anisotropic parameters (except θ) and event depths

have multi-modal features and exhibit significant errors from true values. Anisotropic parameters become highly correlated (with correlation coefficients > 0.96) after the inclusion of perforation-shot depths in the inversion, and the posterior marginals for depths between different perforation shots exhibit even higher correlation coefficients (close to 1). As a result, the strong correlation between model parameters leads to poor posterior estimates.

In conclusion, the simulation study demonstrates that the inversion algorithm is robust to a broad range of noise levels as long as the observed noise statistics are consistent with the assumed noise statistics in the inversion. In addition, assuming HTI anisotropy in ORT media may cause biases for microseismic event locations.

Effects of array aperture on inversion results

All the above simulations are based on known origin times for both perforation shots and microseismic events, which is not the case for practical microseismic data processing. In the absence of available origin times, the aperture of the monitoring array is one of the key factors that affect the resolution of located microseismic events, and larger apertures result in better resolution (Duncan and Eisner, 2010; Eaton, 2018). In practice, the star arrays often have diameters of twice the target depth. However, Fish (2012) found that, to accurately image a target by surface-microseismic monitoring, the minimal aperture needed is a function of formation velocities, geologic structure, dip, economics, etc.

To examine effects from the array aperture size on inversion results, we carry out a series of simulations with ORT model using various array geometries. The ratio of array radius to maximal event depth ranges from 0.9 to 2.3 with an increment of 0.2. We choose 0.9 as the starting ratio since it represents the physical modelling case in Figure 1. In simulations, we use the same true model parameters presented in above simulations to generate datasets. Zero-mean Gaussian noise is added to the theoretical P-wave first arrival times to simulate picking errors. In the Bayesian inversion, origin times for perforation shots and microseismic events are taken as extra model parameters.

Figure 6 presents marginal distributions for model parameters obtained with three representative aperture sizes (i.e., with array ratios of 0.9, 1.9, 2.3). In the absence of the precise knowledge of origin times prior to inversion, reliable epicentre locations can still be obtained, and a larger aperture size tends to yield narrower marginal distributions for epicentres (shown in Figure 6 (b)). Whereas, for a ratio of 0.9, both retrieved velocity parameters (except the parameter θ) and origin times are poor and exhibit multi-modal features. In this case, microseismic-event depths have the largest uncertainty and exhibit large errors from true values. As the array ratio increases, multi-modality and uncertainty are substantially reduced. When the ratio exceeds 1.9, model parameters are resolved with relatively small errors around the mode of marginal distributions and modes agree with true values. For a ratio of 1.9, depth uncertainty is lower, and mode values are much closer to true values. For a ratio of 2.3, multi-modality further diminishes. Although secondary modes still exist, depth and origin-time resolutions appear sufficient for $r = 2.3$.

In terms of the correlation matrices of posterior marginals for anisotropic parameters (except θ) and perforation-shot origin times, all these modal parameters especially origin

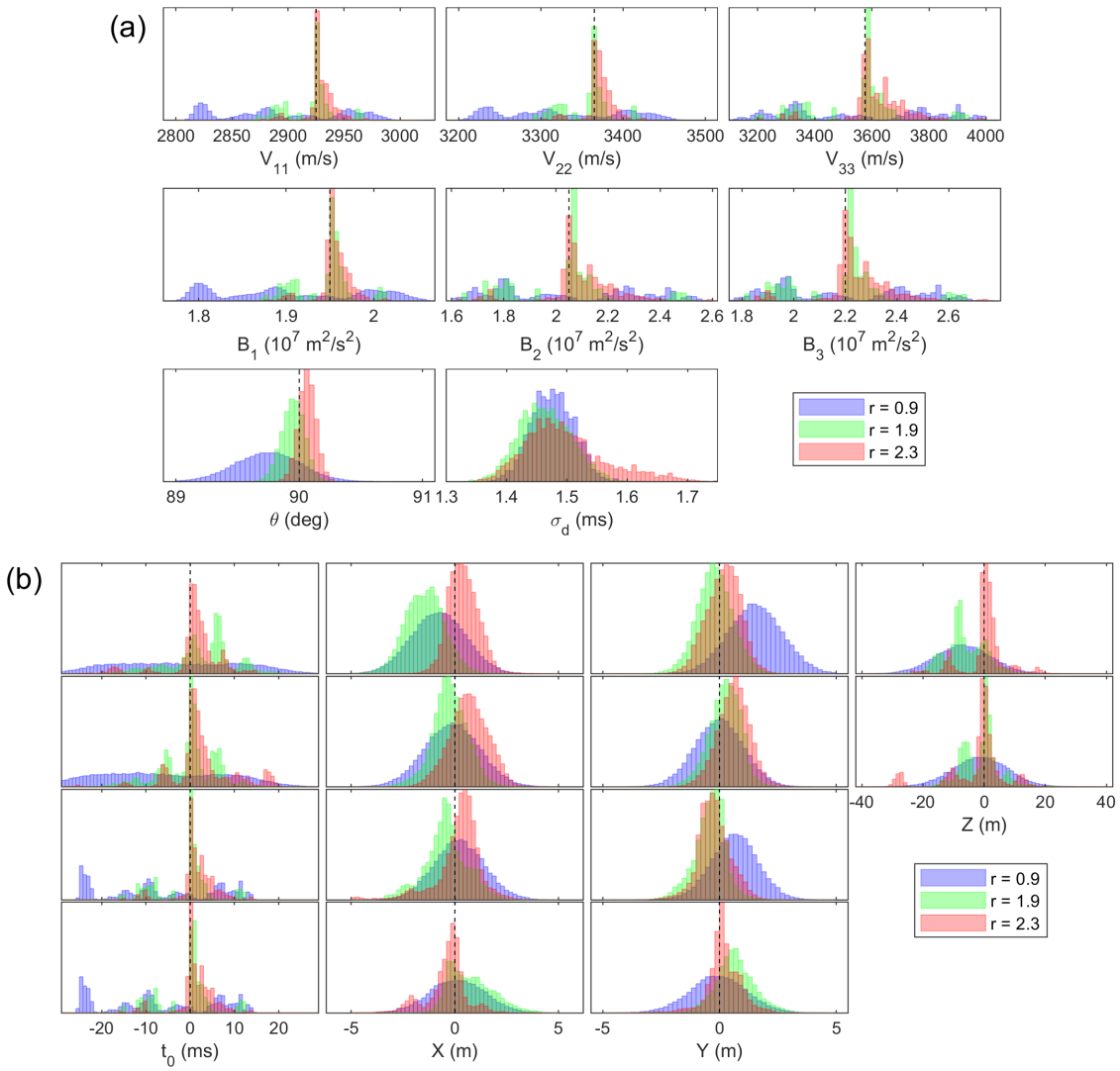

FIG. 6. Marginal distributions of model parameters for three representative array ratios (i.e., 0.9, 1.9, 2.3). (a) Marginals of anisotropic parameters, noise standard deviation. (b) Marginals of absolute errors in origin times and hypocentres for two typical microseismic events (the first two rows) and marginals of origin times and epicentres for two typical perforation shots (the last two rows).

times are strongly correlated. For a ratio of 0.9, correlation coefficients between origin times are close to 1. Thus, the model with a small aperture size tends to overfit the dataset and exhibits multi-modal features. While with the increase of aperture size, the correlation between origin times is gradually reduced, which can help provide more independent information in the inversion and overcome the overfitting problem. Compared with the ORT model, the isotropic velocity model conventionally used in practically microseismic data processing has significantly less parameters. Thus, it is unlikely to produce overfitting results even with a small aperture size.

Triggered perforation shots

The above simulation indicates that, in the absence of precise event origin times, resolving event depths and anisotropic parameters of ORT media requires large array apertures (e.g., array ratios ≥ 2.3 in the simulation case), which may not be practical in the field. Here, we present a simulation to investigate if the triggered perforation shots (i.e., with known origin times) can ease the requirements for aperture size.

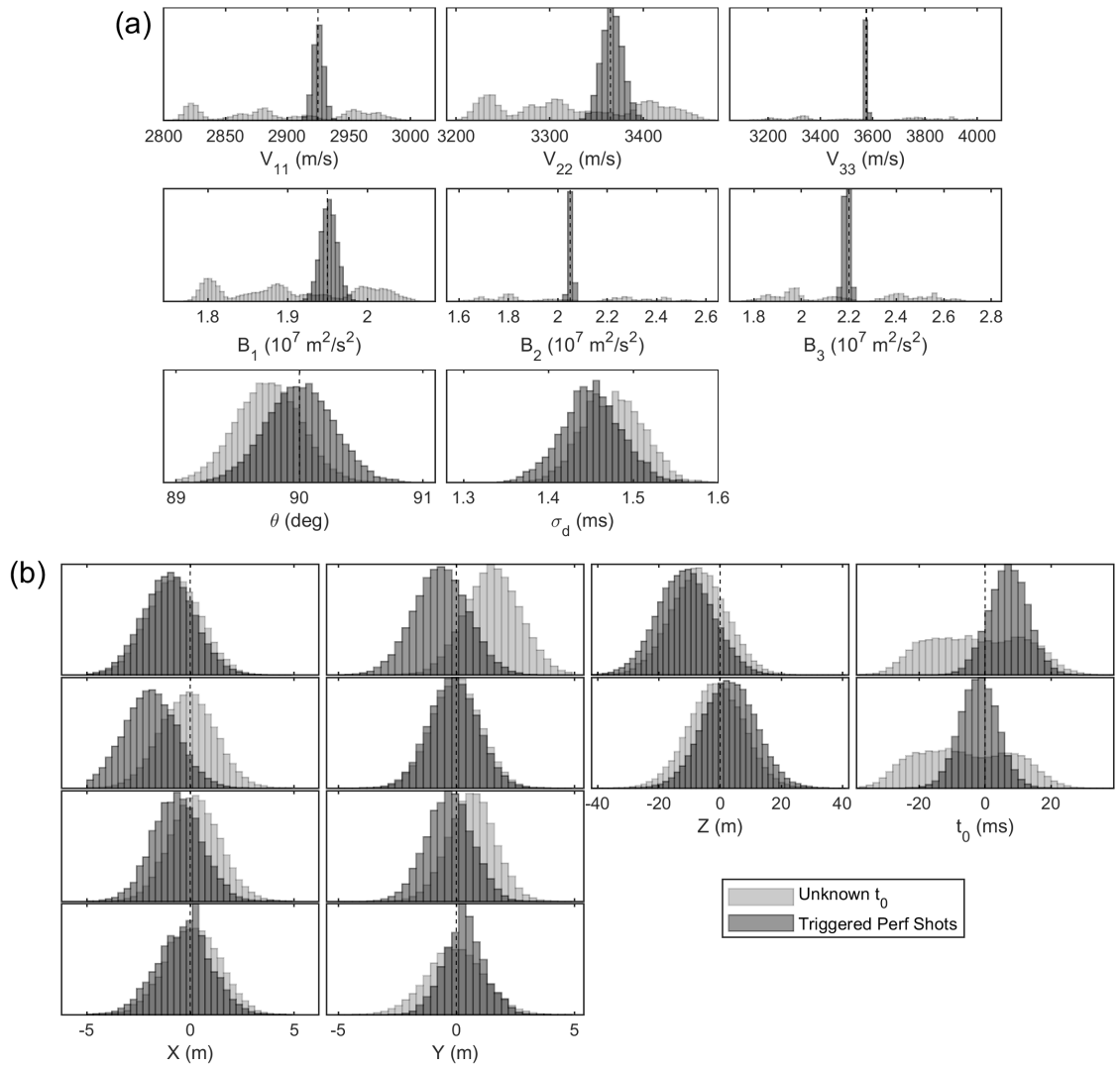

FIG. 7. Marginal distributions of model parameters for the case with triggered perforation shots (shown in dark grey colour). (a) Marginals of anisotropic parameters and noise standard deviation. (b) Marginals of absolute errors in origin times and event hypocentres for two typical microseismic events (the first two rows) and marginals of epicentres for two typical perforation shots (the last two rows). For the sake of comparison, the results with unknown origin times for perforation shots are also plotted (in light grey colour).

In this simulation, we use the same model parameters to above simulations and the same acquisition geometry in Figure 1 with an array ratio of 0.9. Origin times are assumed to be known for perforations shots and unknown for microseismic events. As shown in Figure

7, all the model parameters can be well resolved for the case with triggered perforation shots, and posterior marginals exhibit Gaussian-like distributions. For all the events, the MAP estimates of locations and origin times are highly consistent with true values and exhibit only minor deviations from the true values. Similar to the results with unknown origin times (in light grey colour in Figure 7), event depths also exhibit larger uncertainties than epicentres. In addition, compared with above simulations that have unavailable origin times for perforation shots, the correlation coefficients between marginals of anisotropic parameters are significantly decreased. Therefore, the use of triggered perforation shots could ease the requirements for array apertures and help eliminate the multi-modality of marginal distributions at small array apertures, leading to better microseismic catalogs.

Hybrid monitoring array

In addition to star-array aperture and the triggered perforation shots, we also examine the effects of an additional downhole array within the anisotropic layer when the array ratio is 0.9. The vertical array was placed at x=-400 *m* and y= -200 *m*, consisting of 10 receivers at depths from 420 *m* to 600 *m* with 20-*m* spacing. Due to the inability of surface arrays to precisely resolve perforation-shot depths in simultaneous inversion, the depths of perforation shots are fixed in the previous numerical and physical modelling studies. In the case considered here, in addition to origin times of both perforation shots and microseismic events, perforation-shot depths are also considered as unknown parameters. As shown in Figure 8, depths of both perforation shots and microseismic events are estimated robustly, with the length of 95% CIs typically less than 60 *m*. In addition, all other model parameters are also well resolved and do not show multiple modes. We conclude that vertical array provides important information when deployed together with surface arrays. In particular, the vertical array improves depth and origin time resolution, adding significant robustness to the data information.

RESULTS FOR PHYSICAL MODELLING DATA

In this section, we first consider results of two Bayesian inversions for laboratory data recorded with the phenolic block using the HTI and ORT models, respectively. Since origin times are known at time zero for the experiment, we first apply simultaneous inversion with known origin times for both perforation shots and microseismic events. Figures 9 presents the posterior marginal distributions for anisotropic parameters and noise standard deviations for the HTI and ORT cases, which appear Gaussian-like. At the stage of setting up the acquisition geometry, the HTI symmetry axis and the ORT x_1 axis were placed at approximately 90° from the x axis of the acquisition coordinates. The retrieved HTI and ORT θ values are very close to this value, with modes of posterior marginals at $\sim$88.8°. In both HTI- and ORT-medium assumptions, three velocities are estimated by the inversion, i.e., V_0, V_{45}, V_{90}, and V_{11}, V_{22}, V_{33}. Most velocity estimates have narrow uncertainties, less than 60 *m/s* in terms of 95% CIs. However, uncertainties for V_0 and V_{22} are broader. In the ORT model, B_1, B_2 and B_3 are also used and posterior marginals are shown in Figure 9 (b). Estimated noise standard deviations for both inversions are shown in Figure 9 (c), with modes of posterior marginals at 3.9 *ms* and 1.9 *ms* for the HTI and ORT models, respectively. This result indicates that the ORT model produces significantly better fit to the data.

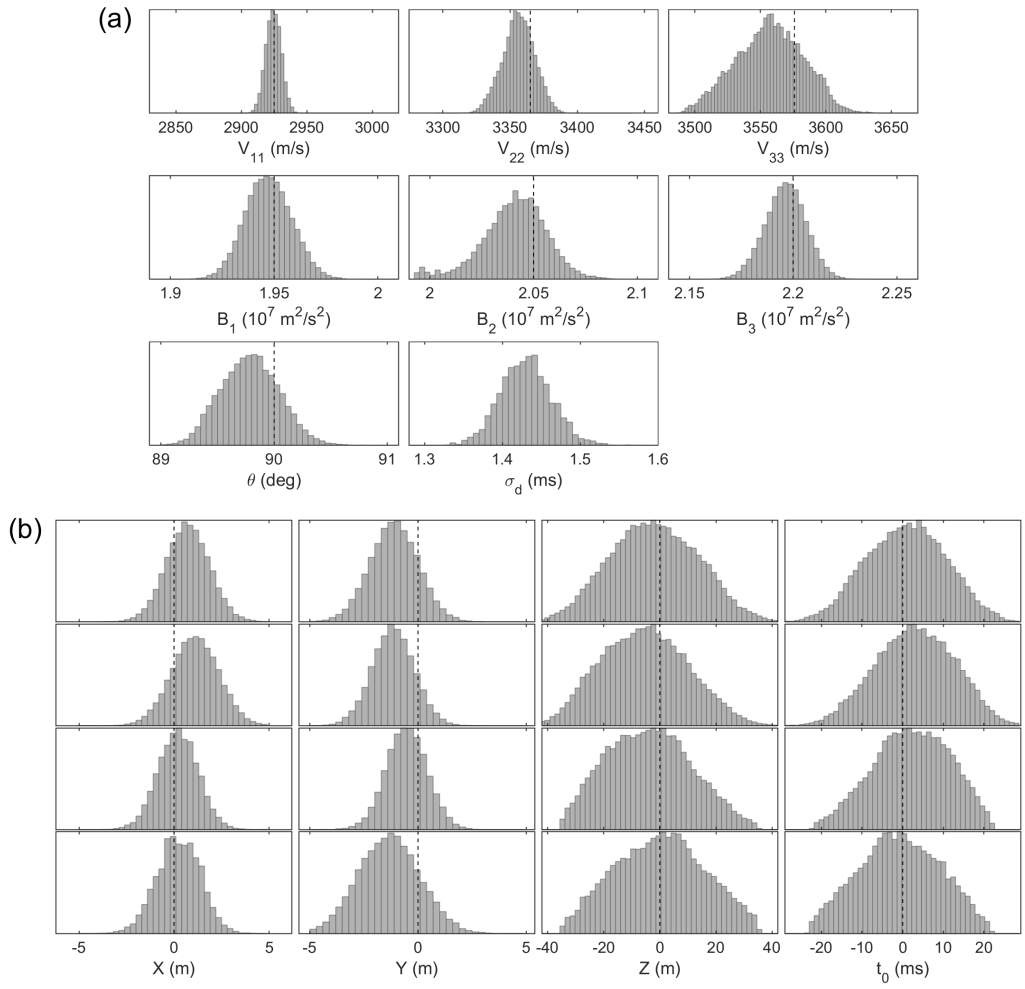

FIG. 8. Marginal distributions of model parameters with the hybrid monitoring array. (a) Marginals of anisotropic parameters and noise standard deviation. (b) Marginals of absolute errors in origin times and event locations for two typical microseismic events (the first two rows) and two typical perforation shots (the last two rows).

Similar to the simulation study in Figure 5, we also estimate P-wave first arrival times for all perforation shots and microseismic events using the MAP model parameters and compute residuals for both inversions. Figure 10 (a) shows residual histograms for both inversions, exhibiting highly similar features to the simulation results in Figure 5. The 95% CIs of the arrival-time residuals for HTI and ORT models are [-5.7, 4.3] *ms* and [-2.7, 2.6] *ms*, respectively. The results with ORT model appear unbiased and the residual histogram is Gaussian-like. In contrast, the distribution with HTI model is non-zero mean and asymmetric. Based on the standard deviation results and the residual analysis, we conclude that the ORT model causes significantly less theory error and is the preferable model to study the phenolic CE material. Figure 10 (b) shows waveforms at one receiver line for a typical event with picked and modelled P-wave first arrivals. Compared with picked arrival times, the modelled HTI arrival times are larger at small offsets and smaller at large offsets, which implies an averaging effect. The modelled arrival times for the ORT medium exhibit much better match with the picked arrival times at all stations.

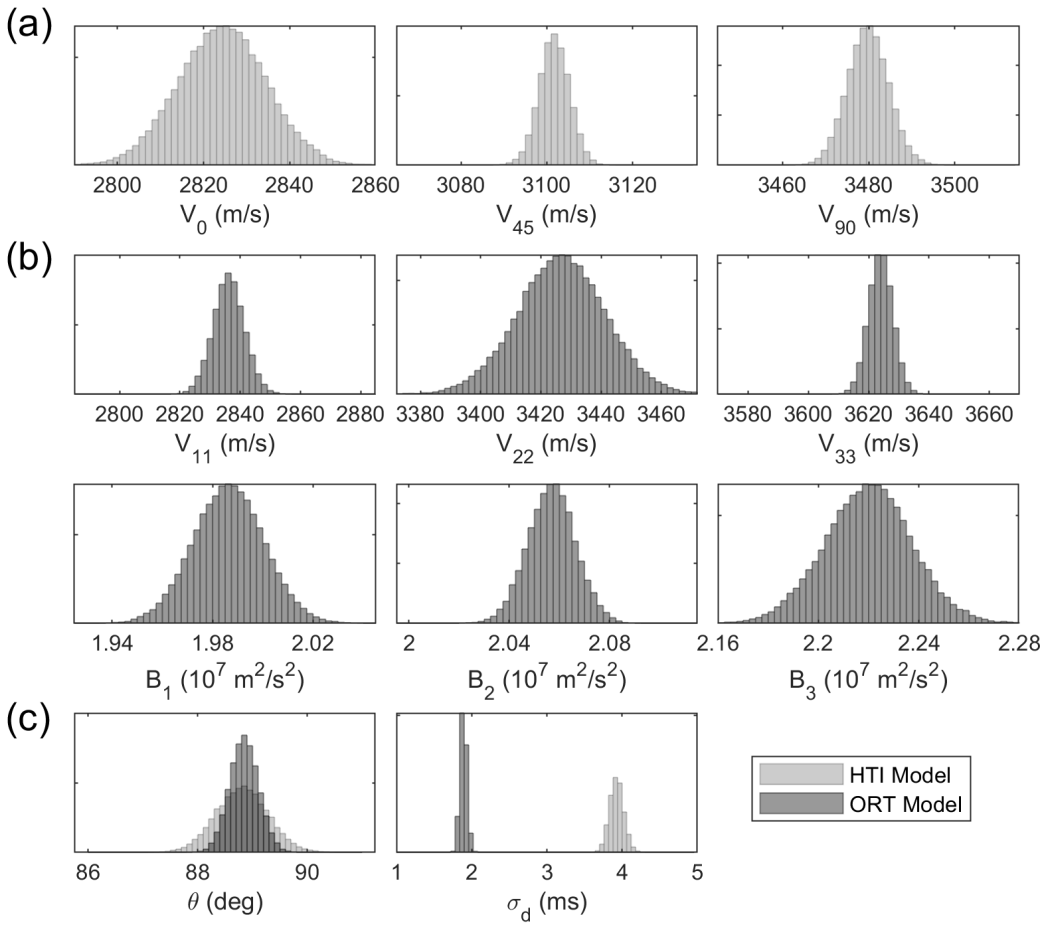

FIG. 9. Marginal distributions for estimated anisotropic parameters (except θ) of (a) HTI model and (b) ORT model, (c) deviation angles (θ) of symmetry axis and x_1 axis from the x axis in the coordinate system as well as the noise standard deviation (σ_d).

The poor performance of the HTI model can be further understood. The inverted HTI symmetry axis and ORT x_1 axis deviate from the x axis by 88.8°(Figure 9 (c)), i.e., are approximately aligned with the y axis of data acquisition. Under the Byun approximation (Byun et al., 1989), velocities along the y and z axes are the same due to the same angle with respect to the symmetry axis. However, for the ORT model, velocities along the three axes can be assigned different values, and the inclusion of the B_i parameters further aids data fit. The velocities along the three axes for a phenolic CE material differ with a $\sim$200-*m/s* difference of velocities along the y and z axes (Cheadle et al., 1991), and is consistent with a weak ORT medium. The HTI assumption ignores the $\sim$200-*m/s* difference, leading to significant arrival-time misfits. For stronger anisotropy, the data residuals for the HTI model are expected to degrade further. This physical modelling example implies that ignoring horizontal layering in the presence of vertically aligned fractures can result in significant event-location errors.

Results are also considered in terms of estimated event locations for both inversions and those recorded during the experiment. Figure 11 presents epicentre marginals for eight per-

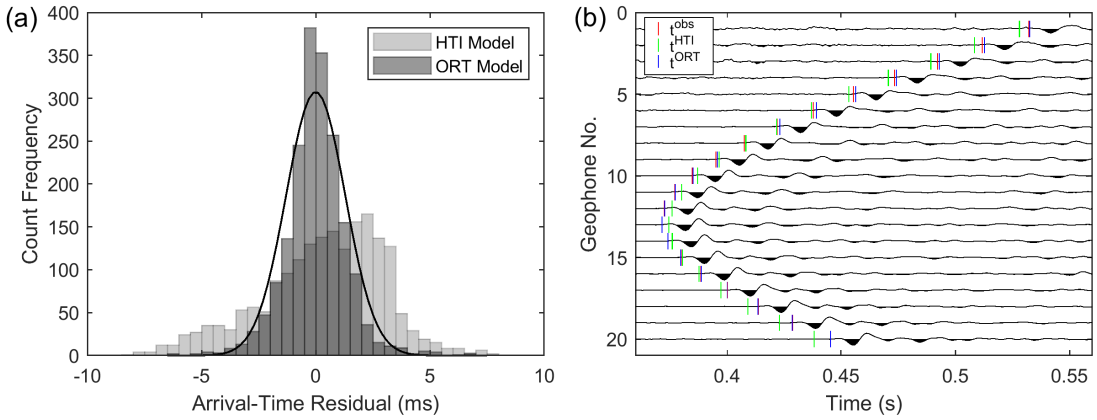

FIG. 10. Arrival-time residuals using HTI-medium and ORT-medium approximations. (a) Histograms of arrival-time residuals using HTI and ORT models. (b) Comparison between picked P-wave first arrivals (red lines) and modelled arrival times with approximated HTI (green lines) and ORT (blue lines) media. The waveforms plotted were recorded at one receiver line for a typical event. In figure (a), the best-fitting Gaussian distribution for the result with ORT model is represented by the black line.

foration shots and 11 microseismic events. The ORT medium yields significantly smaller epicentre uncertainties compared to those obtained under the HTI approximation. For example, the 95% CIs average 14.4 *m* for HTI and 6.5 *m* for ORT models along the x direction, and 10.2 *m* and 4.8 *m* along the y direction. Figure11 also shows event positions recorded during the experiment. A systematic shift exists between inversion estimates and recorded positions for both inversions especially along y direction. Figure 11 (c) shows an enlargement of an epicentre estimate for a single event that illustrates the shift clearly. The shifts are on average 12.6 *m* and 11.9 *m* in y direction for HTI and ORT models, respectively. The systematic shifts are easier to be observed in the marginal distributions of residuals in hypocentres in Figure 12. These shifts are mainly caused by measurement errors due to the sizes of the piezoelectric pins. In addition, when the piezoelectric pins move to a new position, there will be a minor vibration at the pins. But the acquisition system starts the signal firing and recording for a new microseismic event before the pins are fully stabilized. Thus, the minor vibration associated with the two pins is also a source of error.

Epicentre estimates with the HTI and ORT models differ most significantly in the x-direction for the four events on the far right. For these events, the x locations from the HTI model are shifted to the right of the recorded locations (8.2-*m* difference on average). The ORT-model results are closer to the recorded locations and located slightly on the left of the recorded values (2.1-*m* difference on average). This location discrepancy is consistent with our simulation study and likely due to the HTI model's deficiency to appropriately characterize the phenolic CE material.

In terms of marginal distributions of residuals in event depths shown in Figure 12, the HTI model yields significantly larger depth uncertainty than the ORT model. The HTI model also produces shallower source depths, which is also consistent with the simulation study. The ORT model estimates depths to be slightly deeper than the recorded values. This systematic deviation is likely caused by the measurement error due to the piezoelectric-pin size.

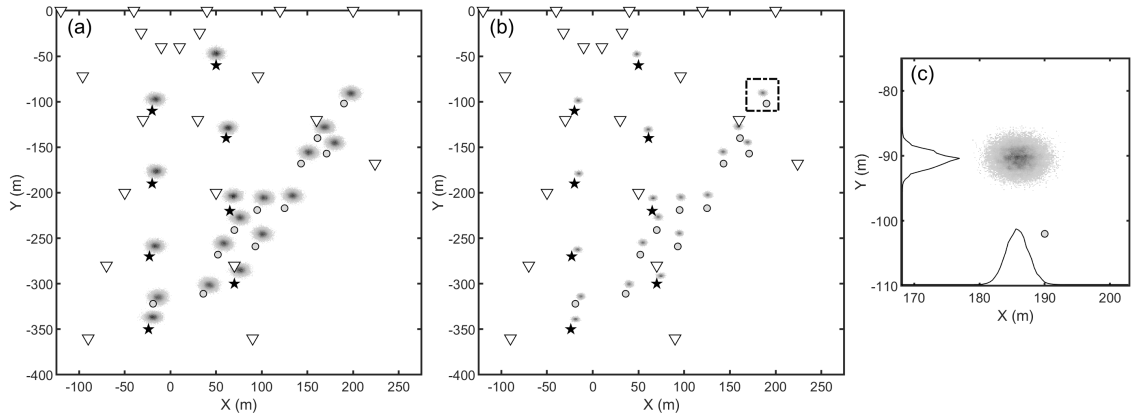

FIG. 11. Epicentre marginal distributions for (a) HTI-model inversion and (b) ORT-model inversion. (c) An enlargement of the red box in (b) with 1D marginals along the x and y axes. All other symbols are as in Figure 1.

The analysis thus far is based on known origin times for perforation shots and microseismic events, which is not the case for field data. Here, we consider inversions with unknown origin times for the ORT model. Figure 13 (b) (the first column and in blue colour) show marginal distributions of origin-time residuals from true values recorded during data acquisition. The distributions are strongly asymmetric and multi-modal for the eight perforation shots. Although origin-time marginals for microseismic events exhibit single modes, the distributions are asymmetric and have large uncertainties. For all events, MAP estimates for origin times exhibit significant discrepancies with true values, and are positive, up to 20 *ms*. Strong correlations between marginal distributions of anisotropic parameters and perforation-shot origin times are also observed. Figure 13 (a) presents the estimates of anisotropic parameters and standard deviation (in blue colour). Compared to the results with known origin times (in green colour), we observe that the deviation angle θ differs only slightly between inversions with known and unknown origin times. All other model parameters now display strongly non-Gaussian and multi-modal features, and very large uncertainties. However, data are well fit (noise standard deviation MAP value of 1.55 *ms*), suggesting insufficient data constraints due to an unfavorable acquisition geometry.

In addition to event origin times, Figure 13 (b) also display marginals for event locations. Although both inverted origin times and velocity parameters have prominent deviations, marginals of horizontal locations for the two sets of results (in green and blue colours) only exhibit slight difference for some individual perforation shots, and no noticeable differences are observed for horizontal locations of microseismic events, which indicates the robustness of the inversion for horizonal locations under the star-shaped surface array. In contrast, depth uncertainties are significantly increased with average 95% CIs of 34.2 *m*, compared to 1.6 *m* when assuming known origin times. In addition, mode values deviate from recorded values by $\sim$9 *m* on average.

Based on the above physical modelling results, we show that reliable epicentre locations can be obtained, even in the absence of known origin times. However, velocity parameters exhibit significant errors for the case with unknown origin times and a small array aperture, resulting in large depth uncertainty. According to our previous simulation results, a large

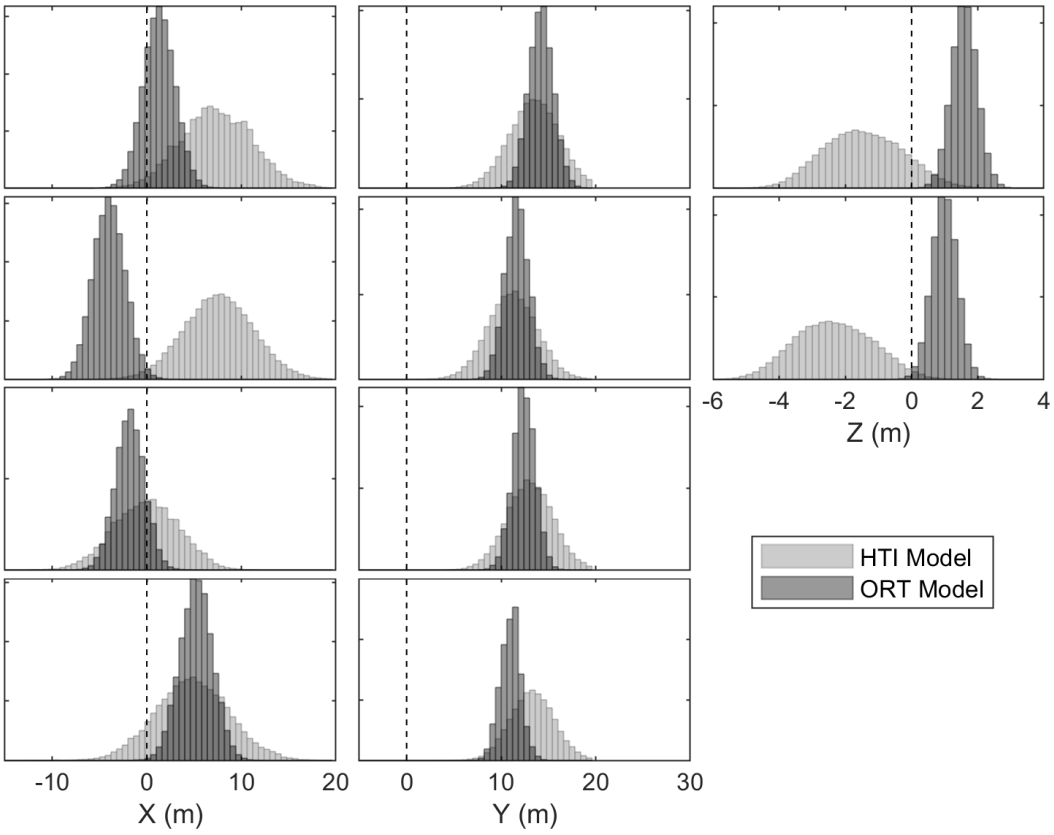

FIG. 12. Marginals of absolute errors in hypocentres for two typical microseismic events (the first two rows) and epicentres for two typical perforation shots (the last two rows).

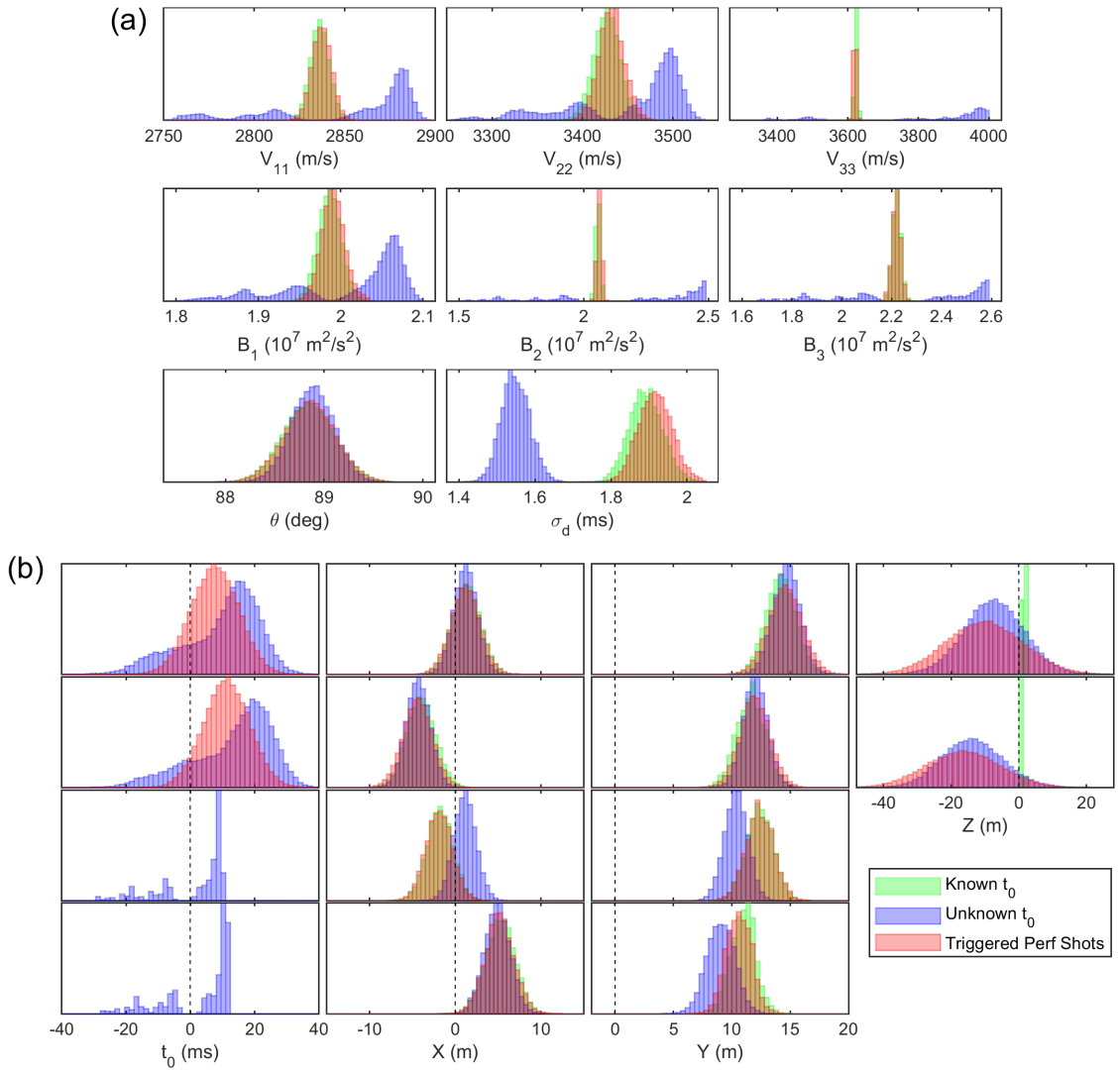

FIG. 13. Marginal distributions of model parameters with known (in green colour) and unknown (in blue colour) origin times for all events as well as triggered perforation shots (in red colour). (a) Marginals of anisotropic parameters, noise standard deviation. (b) Marginals of absolute errors in origin times and event locations for two typical microseismic events (the first two rows) and two typical perforation shots (the last two rows). For the sake of comparison and display, marginal distributions for event depths obtained with known origin times are scaled to proper ranges.

aperture size may help resolve these model parameters. However, due to practical constraints (the size of the phenolic block), we cannot acquire more physical modelling data with larger array apertures. Similar to the simulation study, we also carry out the inversion for the laboratory data with triggered perforation shots, and the marginals of model parameters are also shown in Figure 13 (in red colour). The results demonstrate that, in addition to horizontal locations, both microseismic-event origin times, depths and anisotropic parameters can be well resolved. In comparison, the event depths exhibit larger uncertainties than horizontal locations. These results are all in good agreements with our simulation results.

DISCUSSION AND CONCLUSIONS

Model selection

With both synthetic and laboratory datasets, we have carried out a series of Bayesian inversions with HTI or ORT models under different assumptions. To quantitatively evaluate results retrieved with these models, the deviance information criterion (DIC) (Spiegelhalter et al., 2002) is used here. A lower DIC indicates a greater support from the data for the corresponding model. For the model $\mathbf{m_j}$, the DIC is defined as

$$\mathrm{DIC} = D(\hat{\mathbf{m}}_{\hat{\mathbf{j}}}) + 2P_D, \tag{16}$$

where the MAP model is selected to be the characteristic model $\hat{\mathbf{m}}_{\hat{\mathbf{j}}}$ in this study, and the posterior deviance D is defined as

$$D(\mathbf{m_j}) = -2\log L(\mathbf{m_j}). \tag{17}$$

The effective number of parameters P_D in equation (16) is evaluated as P_D = $\bar{D}(\mathbf{m_j})$ - $D(\hat{\mathbf{m}}_{\hat{\mathbf{j}}})$, where $\bar{D}(\mathbf{m_j})$ is the mean posterior deviance.

Previous sections mainly present inversion results for the ORT model. For the sake of comparison, inversions are also conducted with the HTI model. We calculate DIC values for both results using synthetic and laboratory data with the acquisition geometry shown in Figure 1. In the inversion, three different assumptions are considered, i.e., known origin times for both perforation shots and microseismic events, unknown origin times for both perforation shots and microseismic events as well as triggered perforation shots. Table 1 shows the DIC values for all the models considered. We observe that, under the same assumption about origin times, the ORT model always has lower DIC values than the HTI model. Therefore, the ORT model is always the preferred choice to characterize the anisotropic medium.

Within the group of ORT-based inversions, the DIC provides less clear model selection. Although poor inversion results were obtained for the ORT case with unknown origin times and a small-aperture array, the DIC values are lowest for this case based on the physical modelling data. For the simulated data, the three ORT-based inversions produce nearly identical DIC values. It is likely that theory errors exist in the laboratory data which cause the apparent preference for the model with unknown origin times.

Concluding remarks

We have presented a probabilistic approach to simultaneously estimate microseismic event locations and elastic properties in anisotropic media caused by the presence of vertically aligned fractures in finely horizontally layered media. The inversion rigorously quantifies parameter uncertainties by treating locations for microseismic events, horizontal locations of perforation shots, effective anisotropic parameters, and the noise standard

Table 1. DIC values of different models for simulated and laboratory datasets.

Anisotropic Model		With Known t_0		With Unknown t_0		Triggered Perf Shots	
		HTI	ORT	HTI	ORT	HTI	ORT
DIC	Synthetic Data	-9.507E+3	-1.144E+4	-1.087E+4	-1.142E+4	-9.694E+3	-1.143E+4
	Laboratory Data	-9.535E+3	-1.092E4	-1.087E+4	-1.129E+4	-9.694E+3	-1.090E4

deviation as unknown. Two forward models are considered. The ORT model presents the preferred anisotropy parametrization since it accounts for fractures- and layering-caused anisotropy. It applies a linear approximation for group velocities. A simpler HTI model applies the Byun approximation and illustrates the effects of model simplification (i.e., it ignores horizontal-layering induced VTI). The simultaneous inversion approach has been applied to both simulated and physical modelling datasets. In the physical modeling experiment, a phenolic CE layer is approximately considered as an anisotropic medium, and an analog of star-like surface array is used to recorded waveforms of simulated microseismic events and perforation shots. Both inversions with simulated and physical modelling data imply that, in the real data processing, the ignorance of VTI caused by horizontal layering in a fractured reservoir may lead to systematic event-location errors. With known origin times, inversion results indicate that the use of ORT-medium approximation could yield event locations with less uncertainty and could lead to much smaller P-wave arrival-time misfit than that obtained with the HTI-medium approximation. Furthermore, the inversion can also account for measurement errors within the recorded perforation-shot locations by assigning them priors with narrow ranges, and the proposed algorithm can place them into more reliable locations. In addition, the Bayesian inversion has also been applied to a case closer to conventional microseismic data processing, in which no precise origin times are available prior to inversion. By considering origin times as extra unknowns with ORT-medium assumption for the phenolic block, reliable horizontal locations could still be yielded, while posterior distributions for both velocity parameters and origin times exhibit asymmetric, multi-modal features and relatively large deviations from the recorded values. Compared with the case with known origin times, posterior distributions of event depths also exhibit larger uncertainty and the MAP estimates deviate more from the recorded ones. Meanwhile, the inverted model parameters in this case were found to overfit the observed data resulting in a smaller arrival-time misfit. These simulations reveal that the aperture size of the star-shaped array plays a key role for yielding robust results. Resolving event depths as well as anisotropic parameters of ORT medium requires certain array aperture. With the increase of aperture size, posterior distributions of model parameters are likely to exhibit less asymmetric and multi-modal features. Using the similar model-parameter setup as in the physical modelling experiment, reliable model parameters could be retrieved when the ratio of array radius to maximal event depth exceeds 2.3, while such a large array ratio may be impractical for in-the-filed monitoring system design. Moreover, we have also carried out inversions with known perforation-shot origin times (i.e., triggered perforation shots). For simulated and laboratory datasets, consistent results have been obtained that both event depths and anisotropic parameters are well resolved for the case of triggered perforation shots. Therefore, the information about precise perforation shot timing eases requirements for the aperture size of the star-shaped array. Besides, a simulation study also demonstrates

that the inclusion of a downhole array to the star-like surface array also help resolve for stable inversion results, and the perforation-shot depths can also be robustly estimated with the hybrid array. Synthetic examples presented in this work can help provide insights into in-the-field monitoring system design.

ACKNOWLEDGEMENTS

We thank the sponsors of CREWES for continued support. This work was funded by CREWES industrial sponsors, NSERC (Natural Sciences and Engineering Research Council of Canada) through the grants CRDPJ 461179-13 and CRDPJ 543578-19. Partial funding also came from the Canada First Research Excellence Fund. We are grateful for the help from Kevin Bertram to set up physical models.

REFERENCES

Akram, J., and Eaton, D. W., 2016, A review and appraisal of arrival-time picking methods for downhole microseismic dataarrival-time picking methods: Geophysics, **81**, No. 2, KS71–KS91.

Akram, J., and Eaton, D. W., 2017, 1d layered velocity models and microseismic event locations: synthetic examples for a case with a single linear receiver array: Journal of Geophysics and Engineering, **14**, No. 5, 1215–1224.

Baig, A., and Urbancic, T., 2010, Microseismic moment tensors: A path to understanding frac growth: The Leading Edge, **29**, No. 3, 320–324.

Bakulin, A., Grechka, V., and Tsvankin, I., 2000, Estimation of fracture parameters from reflection seismic data—part i: Hti model due to a single fracture set: Geophysics, **65**, No. 6, 1788–1802.

Blias, E., and Grechka, V., 2013, Analytic solutions to the joint estimation of microseismic event locations and effective velocity model: Geophysics, **78**, No. 3, KS51–KS61.

Block, L. V., Cheng, C. H., Fehler, M. C., and Phillips, W. S., 1994, Seismic imaging using microearthquakes induced by hydraulic fracturing: Geophysics, **59**, No. 1, 102–112.

Byun, B. S., Corrigan, D., and Gaiser, J. E., 1989, Anisotropic velocity analysis for lithology discrimination: Geophysics, **54**, No. 12, 1564–1574.

Cameron, M. K., Fomel, S. B., and Sethian, J. A., 2007, Seismic velocity estimation from time migration: Inverse Problems, **23**, No. 4, 1329.

Cheadle, S. P., Brown, R. J., and Lawton, D. C., 1991, Orthorhombic anisotropy: A physical seismic modeling study: Geophysics, **56**, No. 10, 1603–1613.

Chen, G., Song, L., and Liu, L., 2019, 3d numerical simulation of elastic wave propagation in discrete fracture network rocks: Pure and Applied Geophysics, **176**, No. 12, 5377–5390.

Chen, Z., Cox, B., and Perkins, C., 2013, The influence of hti anisotropy on microseismic event location—a case study from a tight gas field in british columbia, *in* SEG Technical Program Expanded Abstracts 2013, Society of Exploration Geophysicists, 2003–2007.

Chichinina, T., Dugarov, G., and Obolentseva, I., 2013, Fracture-induced q-anisotropy: Inversion for fracture parameters, *in* SEG Technical Program Expanded Abstracts 2013, Society of Exploration Geophysicists, 335–340.

Daley, P. F., and Krebes, E. S., 2016, A linearized group velocity approach for two-point qp ray tracing in a layered orthorhombic medium: Journal of Seismic Exploration, **25**, No. 1, 87–101.

Dettmer, J., and Dosso, S. E., 2012, Trans-dimensional matched-field geoacoustic inversion with hierarchical error models and interacting markov chains: The Journal of the Acoustical Society of America, **132**, No. 4, 2239–2250.

Dosso, S. E., Dettmer, J., Steininger, G., and Holland, C. W., 2014, Efficient trans-dimensional bayesian inversion for geoacoustic profile estimation: Inverse Problems, **30**, No. 11, 114,018.

Duncan, P. M., and Eisner, L., 2010, Reservoir characterization using surface microseismic monitoring: Geophysics, **75**, No. 5, 139–146.

Earl, D. J., and Deem, M. W., 2005, Parallel tempering: Theory, applications, and new perspectives: Physical Chemistry Chemical Physics, **7**, No. 23, 3910–3916.

Eaton, D. W., 2018, Passive seismic monitoring of induced seismicity: Fundamental principles and application to energy technologies: Cambridge University Press.

Eaton, D. W., and Forouhideh, F., 2011, Solid angles and the impact of receiver-array geometry on microseismic moment-tensor inversion: Geophysics, **76**, No. 6, WC77–WC85.

Eisner, L., Duncan, P. M., Heigl, W. M., and Keller, W. R., 2009, Uncertainties in passive seismic monitoring: The Leading Edge, **28**, No. 6, 648–655.

Eisner, L., Hulsey, B. J., Duncan, P., Jurick, D., Werner, H., and Keller, W., 2010, Comparison of surface and borehole locations of induced seismicity: Geophysical Prospecting, **58**, No. 5, 809–820.

Erwemi, A., Walsh, J., Bennett, L., Woerpel, C., and Purcell, D., 2010, Anisotropic velocity modeling for microseismic processing: Part 3—borehole sonic calibration case study, *in* SEG Technical Program Expanded Abstracts 2010, Society of Exploration Geophysicists, 508–512.

Eyre, T. S., and van der Baan, M., 2017, The reliability of microseismic moment-tensor solutions: Surface versus borehole monitoringmoment-tensors: Surface vs. borehole: Geophysics, **82**, No. 6, KS113–KS125.

Fish, A. M., 2012, Microseismic velocity inversion and event location using reverse time imaging: Ph.D. thesis, Colorado School of Mines.

Gesret, A., Desassis, N., Noble, M., Romary, T., and Maisons, C., 2015, Propagation of the velocity model uncertainties to the seismic event location: Geophysical Journal International, **200**, No. 1, 52–66.

Geyer, C. J., 1991, Markov chain monte carlo maximum likelihood.

Grechka, V., 2005, Penny-shaped fractures revisited: Studia Geophysica et Geodaetica, **49**, No. 3, 365–381.

Hirata, N., and Matsu'ura, M., 1987, Maximum-likelihood estimation of hypocenter with origin time eliminated using nonlinear inversion technique: Physics of the Earth and Planetary Interiors, **47**, 50–61.

Hornby, B. E., Schwartz, L. M., and Hudson, J. A., 1994, Anisotropic effective-medium modeling of the elastic properties of shales: Geophysics, **59**, No. 10, 1570–1583.

Husen, S., and Hardebeck, J. L., 2010, Earthquake location accuracy, community online resource for statistical seismicity analysis, doi: 10.5078/corssa-55815573: Available on-line at: http://www. corssa. org.

Jansky, J., Plicka, V., and Eisner, L., 2010, Feasibility of joint 1d velocity model and event location inversion by the neighbourhood algorithm: Geophysical Prospecting, **58**, No. 2, 229–234.

Jarillo Michel, O., and Tsvankin, I., 2017, Waveform inversion for microseismic velocity analysis and event location in vti media: Geophysics, **82**, No. 4, WA95–WA103.

King, A., and Talebi, S., 2007, Anisotropy effects on microseismic event location: Pure and Applied Geophysics, **164**, No. 11, 2141–2156.

Kissling, E., 1988, Geotomography with local earthquake data: Reviews of Geophysics, **26**, No. 4, 659–698.

Kumar, D., Sen, M. K., and Ferguson, R. J., 2004, Traveltime calculation and prestack depth migration in tilted transversely isotropic media: Geophysics, **69**, No. 1, 37–44.

Li, J., Zhang, H., Rodi, W. L., and Toksoz, M. N., 2013, Joint microseismic location and anisotropic tomography using differential arrival times and differential backazimuths: Geophysical Journal International, **195**, No. 3, 1917–1931.

Mahmoudian, F., 2013, Physical modeling and analysis of seismic data from a simulated fractured medium: Ph.D. thesis, University of Calgary.

Maxwell, S. C., Bennett, L., Jones, M., and Walsh, J., 2010, Anisotropic velocity modeling for microseismic processing: Part 1—impact of velocity model uncertainty, *in* SEG Technical Program Expanded Abstracts 2010, Society of Exploration Geophysicists, 2130–2134.

Pavlis, G. L., and Booker, J. R., 1980, The mixed discrete-continuous inverse problem: Application to the simultaneous determination of earthquake hypocenters and velocity structure: Journal of Geophysical Research: Solid Earth, **85**, No. B9, 4801–4810.

Pei, D., Quirein, J. A., Cornish, B. E., Quinn, D., and Warpinski, N. R., 2009, Velocity calibration for microseismic monitoring: A very fast simulated annealing (vfsa) approach for joint-objective optimization: Geophysics, **74**, No. 6, WCB47–WCB55.

Pei, D., Quirein, J. A., Cornish, B. E., Zannoni, S., Ay, E. et al., 2008, Velocity calibration using microseismic hydraulic fracturing perforation and string shot data, *in* SPWLA 49th annual logging symposium, Society of Petrophysicists and Well-Log Analysts.

Piana Agostinetti, N., Giacomuzzi, G., and Malinverno, A., 2015, Local three-dimensional earthquake tomography by trans-dimensional monte carlo sampling: Geophysical Journal International, **201**, No. 3, 1598–1617.

Poliannikov, O. V., Prange, M., Malcolm, A., and Djikpesse, H., 2013, A unified bayesian framework for relative microseismic location: Geophysical Journal International, **194**, No. 1, 557–571.

Poliannikov, O. V., Prange, M., Malcolm, A. E., and Djikpesse, H., 2014, Joint location of microseismic events in the presence of velocity uncertainty: Geophysics, **79**, No. 6, KS51–KS60.

Purba, J. C. S., Dettmer, J., and Gilbert, H., 2020, Nonlinear multiple earthquake location and velocity estimation in the canadian rocky mountain trench: Bulletin of the Seismological Society of America.

Ryberg, T., and Haberland, C., 2019, Bayesian simultaneous inversion for local earthquake hypocentres and 1-d velocity structure using minimum prior knowledge: Geophysical Journal International, **218**, No. 2, 840–854.

Sambridge, M., 1999a, Geophysical inversion with a neighbourhood algorithm—i. searching a parameter space: Geophysical journal international, **138**, No. 2, 479–494.

Sambridge, M., 1999b, Geophysical inversion with a neighbourhood algorithm—ii. appraising the ensemble: Geophysical Journal International, **138**, No. 3, 727–746.

Sambridge, M., 2014, A parallel tempering algorithm for probabilistic sampling and multimodal optimization: Geophysical Journal International, **196**, No. 1, 357–374.

Shapiro, S. A., Dinske, C., and Rothert, E., 2006, Hydraulic-fracturing controlled dynamics of microseismic clouds: Geophysical Research Letters, **33**, No. 14.

Shimoda, N., Reshetnikov, A., and Shaporo, S. A., 2016, Microseismic data processing in shale gas field: Orthorhombic velocity parameter factorizing, hypocenter locating and moment tensor inversion: PHASE Annual Report, 47–72.

Song, L.-P., and Every, A. G., 2000, Approximate formulae for acoustic wave group slownesses in weakly orthorhombic media: Journal of Physics D: Applied Physics, **33**, No. 17, L81.

Spiegelhalter, D. J., Best, N. G., Carlin, B. P., and Van Der Linde, A., 2002, Bayesian measures of model complexity and fit: Journal of the royal statistical society: Series b (statistical methodology), **64**, No. 4, 583–639.

Tan, Y., He, C., and Mao, Z., 2018, Microseismic velocity model inversion and source location: The use of neighborhood algorithm and master station method: Geophysics, **83**, No. 4, KS49–KS63.

Thurber, C. H., 1992, Hypocenter-velocity structure coupling in local earthquake tomography: Physics of the Earth and Planetary Interiors, **75**, No. 1-3, 55–62.

Van Dok, R., Fuller, B., Engelbrecht, L., and Sterling, M., 2011, Seismic anisotropy in microseismic event location analysis: The Leading Edge, **30**, No. 7, 766–770.

Warpinski, N. R., Sullivan, R. B., Uhl, J., Waltman, C., and Machovoie, S., 2005, Improved microseismic fracture mapping using perforation timing measurements for velocity calibration: SPE journal, **10**, No. 01, 14–23.

Warpinski, N. R., Waltman, C. K., Du, J., and Ma, Q., 2009, Anisotropy effects in microseismic monitoring, *in* SPE annual technical conference and exhibition, Society of Petroleum Engineers.

Woerpel, C., 2010, Anisotropic velocity modeling for microseismic processing: Part 2—fast and accurate model calibration with a cross-well source, *in* SEG Technical Program Expanded Abstracts 2010, Society of Exploration Geophysicists, 2135–2139.

Yaskevich, S., and Duchkov, A., 2013, Influence of perforation shot geometry on estimation of anisotropic (hti) parameters in microseismic monitoring, *in* SEG Technical Program Expanded Abstracts 2013, Society of Exploration Geophysicists, 1998–2002.

Yaskevich, S. V., and Duchkov, A. A., 2012, Simultaneous microseismic event location and anisotropic velocity model building in hti media, *in* 74th EAGE Conference and Exhibition incorporating EUROPEC 2012, European Association of Geoscientists & Engineers, cp–293.

Yuan, D., and Li, A., 2017, Joint inversion for effective anisotropic velocity model and event locations using s-wave splitting measurements from downhole microseismic data: Geophysics, **82**, No. 3, C133–C143.

Zhang, F., and Li, X., 2013, Generalized approximations of reflection coefficients in orthorhombic media: Journal of Geophysics and Engineering, **10**, No. 5, 054,004.

Zhang, H., Eaton, D. W., Rodriguez, G., and Jia, S. Q., 2019, Source-mechanism analysis and stress inversion for hydraulic-fracturing-induced event sequences near fox creek, albertasource-mechanism analysis and stress inversion: Bulletin of the Seismological Society of America, **109**, No. 2, 636–651.

Zhang, J., Zhang, H., Zhang, Y., and Liu, Q., 2016, Calibrating one-dimensional velocity model for downhole microseismic monitoring using station-pair differential arrival times based on the differential evolution method: Physics of the earth and planetary interiors, **261**, 124–132.

Zhang, Z., Du, J., and Gao, F., 2018, Simultaneous inversion for microseismic event location and velocity model in vaca muerta formationsimultaneous microseismic inversion: Geophysics, **83**, No. 3, KS23–KS34.

Zhang, Z., Rector, J. W., and Nava, M. J., 2017, Simultaneous inversion of multiple microseismic data for event locations and velocity model with bayesian inference: Geophysics, **82**, No. 3, KS27–KS39.